Turbid Tales:
Where Do Sub-glacial Sediments Go?

Madelaine Gamble Rosevear

October 12, 2018

1 Introduction

1.1 Motivation

At high latitudes, especially around the Antarctic and Greenlandic coastlines, many glaciers terminate in the ocean. Depending on their behaviour sea-ward of the grounding line, these glaciers terminate as either tidewater glaciers, with steep faces, or as ice shelves, with large floating tongues of ice. Water may be present at the bed of a glacier due to *in situ* basal melting, especially if the ice is very thick, or due to surface melt, which can travel to the bed through englacial conduits.

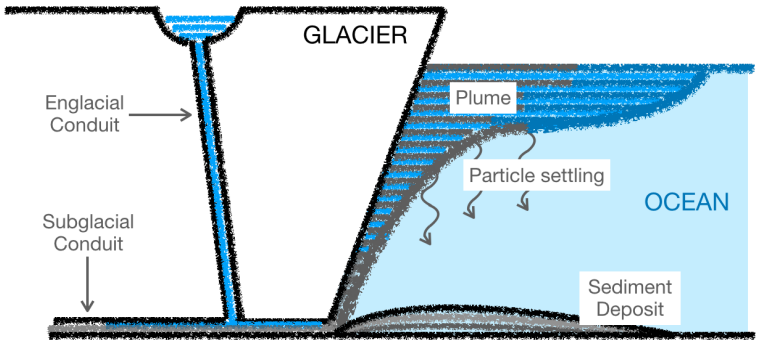

Figure 1: Simple schematic of a glacier terminating in the ocean. Meltwater drains to the bed and enters the ocean at depth, rising to the surface of the ocean as a buoyant plume. Sediments rain out of the plume as it spreads and are deposited on the sea floor.

A considerable amount of glacially eroded sediment is present at the bed, which is entrained into the basal meltwater and transported to the glacier front. The turbid mix of freshwater and sediment that emerges from under the glacier, through one or many channels, is typically less dense than the seawater and rises along the glacier front as a buoyant plume. It may then arrive at the surface (e.g. Fig. 4) or find a level of neutral buoyancy below the surface as its buoyancy evolves with the entrainment of saltwater, the settling of particles, and the addition meltwater from the ice face. Sediments frozen into

the glacier front may also be released as the ice front melts, providing another source of fresh, particle laden fluid.

The velocity, temperature and salinity of a glacial meltwater plume are used in determining the ablation velocity, or rate of melting, of the glacier face. In models of glacier-ocean systems, the ablation velocity is typically parametrised as being proportional to the plume velocity [6], thus the omission of sediments in plume dynamics could have implications for accurate modelling of ablation and making projections of ice sheet mass balance and sea level. Sedimentary records from fjords and beneath ice shelves contain information about ice sheet history [9], however detailed interpretation of these records requires a model linking sediment deposition to to discharge conditions at the grounding line.

1.2 Previous studies

The largest body of relevant literature pertains to turbidity currents, or particle laden gravity currents, which have been studied for their numerous environmental and industrial applications, for example sediment laden rivers entering the ocean, submarine landslides, pyroclastic flows and avalanches. In these instances it is the particles that give the fluid negative buoyancy and drive flow. As the flow evolves, entrainment of ambient fluid and settling of particles will modify the buoyancy of the flow, or remove it alltogether.

Many such studies have considered a particle driven gravity current over a flat bottom [2, 11] however some some have investigated the effect of an inclined bottom [3, 10] and stratification [10], looking at the evolution of gravity current density due to the competing effects of particle settling and the entrainment of ambient fluid and the eventual separation of the current from the slope and intrusion into the ambient. Other studies have looked at the patterns of sediment deposited from particle laden flows such as gravity currents [3] and particle bearing plumes rising vertically in homogeneous [5] and stratified [13] ambients.

One study has developed a model of sedimentation due to subglacial discharge from beneath a vertical ice face [7]. They considered an outflow with sufficient initial momentum that the plume never attached to the ice face; the initial jet like behaviour of the flow carries it away from the ice before buoyancy takes over and the behaviour becomes closer to that of a pure plume. Once the current hits the surface it flows radially as a surface gravity current.

1.3 Overview

The case in which a buoyant, particle bearing plume flows up an inclined ceiling has not been previously studied. Whilst one previous study has investigated sediment deposition due to subglacial discharge [7] they considered distinctly different conditions to those investigated in this study, and have not performed laboratory experiments. Sediment deposition has been measured in some particle laden flows [5, 13], however it has never been studied in this configuration. As such, this study addresses a big gap understanding the effects of slope and particle properties on sediment distribution beneath a sloping "ice" face.

The remainder of the report is arranged as follows. In section 2 we outline the theory developed to explain the observed particle distribution. We then describe the experimental methods used (section 3). In section 4 we show the dependence of particle distribution on the key physical parameters of the study, and apply the theory outlined in section 2.

Finally, we discuss the key results and considerations in a geophysical setting (section 5), and outline the conclusions of the study (section 6).

2 Theory

Figure 1 illustrates the key processes thought to be taking place in the transport and deposition of sediments by a forced line plume rising beneath a model ice shelf in our experiments. The particle laden plume is a mix of fresh water and particles of diameter d_p, density ρ_p and concentration (by volume) ϕ_0. It enters the domain as a forced line plume, assumed to be uniform in the spanwise direction, characterised by Q_0, the volume injected per unit time, per unit width of the domain. In all experiments, the density of the injected fluid is less than the density of the saltwater ambient ρ_a. The line plume enters the domain at a height between z = h_0 and H_0. The domain has a trapezoidal cross-section, with a horizontal lower boundary at $z = 0$ and a sloping upper boundary at $z = H(x) = H_0 + sx$, in which $s = \tan(\theta)$ is the slope corresponding to the upper boundary forming an angle θ to the horizontal. The forced plume enters the domain at $x = 0$ and interacts with the upper and lower boundaries of the tank, forming a recirculating region, which we assume extends to horizontal distance x_r. From this region a particle-bearing plume emerges, which rises along the upper slope. The plume propagates along the slope, entraining the underlying fluid at a rate proportional to the plume speed, while particles settle within the plume at a rate proportional to the Stokes settling velocity. As particles within the plume rain out from its base, they are advected back towards the source by a return flow that results from entrainment of ambient fluid into the recirculating region. Some of these particles rain out onto the bottom while some are carried into the recirculating region where they are recycled into the plume or settle out. In the following sections we consider these dynamics, assuming

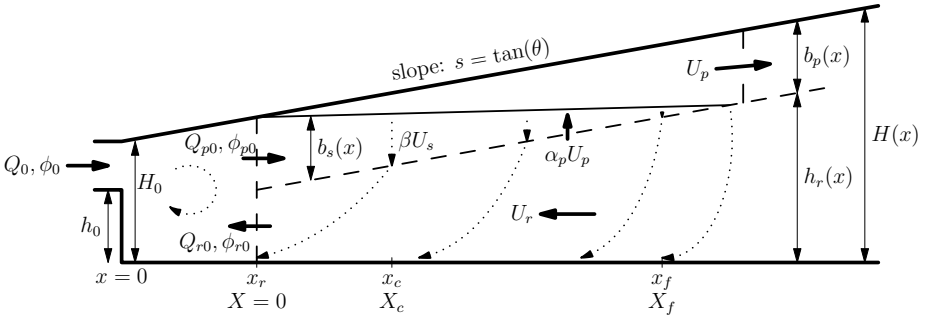

Figure 2: Schematic of the experimental domain with variables defined.

that the system is in steady state. Because the experiments have limited duration, we also consider the effect of particles remaining in the plume after the source has been turned off, and make the assumption that these particles settle vertically onto the bottom of the tank. The mass of settled particles is related to the depth of the particle bed by assuming they settle as loosely packed spheres.

2.1 Recirculating region

The volume flux Q_{p0} and the reduced gravity $g'_0 = g(\rho_a - \rho_{p0})/\rho_0$ set the momentum M_0 and buoyancy F_0 fluxes, per unit width, at the source:

$$M_0 \equiv Q_0^2/b_0, \qquad F_0 \equiv Q_0 g'_0 \tag{1}$$

where $b_0 = H_0 - h_0$ is the vertical extent of the fluid at the source and ρ_{p0} is the density of the plume. The distance over which our forced plume is expected to behave like a jet is found by dimensional analysis of (1), and we take the length of the recirculating region to be twice this:

$$x_r = 2(M_0^3 F_0^2)^{1/3} \tag{2}$$

The plume emerges from the recirculating region at $x = x_r$ with a volume flux per unit width of Q_{p0} and a particle concentration ϕ_{p0}. These are both determined in part by the properties of the return flow, namely the return flow volume flux Q_{r0} and return flow particle concentration ϕ_{r0}. The corresponding mass fluxes, per unit width per unit time, of particles from the source, into the plume, and from the return flow are

$$\dot{m}_0 = \rho_p \phi_0 Q_0, \qquad \dot{m_p}_0 = \rho_p \phi_{p0} Q_{p0}, \qquad \dot{m_r}_0 = \rho_p \phi_{r0} Q_{r0} \tag{3}$$

Within the recirculating region a fraction Δ of particles settle to the base per unit time and are not resuspended. Thus the mass of particles entering the plume is

$$\dot{m}_{p0} = (1 - \Delta)(\dot{m}_0 + \dot{m}_{r0}). \tag{4}$$

Conservation of volume requires that the volume flux into the plume is balanced by the sum of the volume flux into the domain and the return volume flux

$$Q_{p0} = Q_0 - Q_{r0}. \tag{5}$$

Combining (3), (4) and (5) gives an expression for the particle concentration in the recirculating region

$$\dot{\phi_p}0 = (1 - \Delta)(\phi_0 Q_0 + \phi_{r0} Q_{r0})/(Q_0 + Q_{r0}). \tag{6}$$

For which estimates of Q_{r0} and ϕ_{r0} are needed. We assume the former is proportional to Q_0 such that

$$Q_{r0} = \alpha_r Q_0. \tag{7}$$

To find ϕ_{r0} we consider how particles that settle out of the plume are advected back by the return flow. These dynamics are considered in the following section.

2.2 Sediment transport in the along-slope plume

We find that the plume propagates along the slope with near-constant speed U_p, a result that is consistent with [4]. U_p is given by

$$U_p = c(g_0' Q_0)^{1/3} \tag{8}$$

In our experiments, we find that turbulent entrainment into the plume is negligibly small. As such, we ignore the effects of this on particle dynamics. In the absence of entrainment, the volume flux and vertical thickness of the plume are constant along its length and

$$Q_p = Q_{p0}, \qquad b_p = b_{p0} \tag{9}$$

in which we assume the thickness of the plume emerging from the recirculating region is equal to half the depth of the domain at $x = x_r$:

$$b_{p0} = 0.5(H_0 + s x_r). \tag{10}$$

Particles were not observed to stay well mixed within the plume as it propagated along the slope. As a result, particles are assumed to settle within the plume at a rate proportional to the stokes settling velocity U_s

$$U_s = \frac{d^2(\rho_p - \rho_{p0})}{18\nu\rho_{p0}} \tag{11}$$

Thus, whilst the plume has constant vertical extent $b_p = b_{p0}$, the thickness of the layer within the plume that contains particles decreases along-slope according to

$$b_s = b_p - (\beta U_s/U_{px})X = b_p 0 - \beta\gamma X, \tag{12}$$

in which $X = x - x_r$ is the horizontal distance from the recirculating region, $U_{px} = U_p \cos\theta$ is the x projection of the alongslope plume velocity and $0 \leq \beta \leq 1$ is the proportionality constant which is a measure of the turbulent activity within the plume, which determines the capacity for the flow to keep the particles well mixed. If the flow is laminar, we would expect $\beta = 1$, corresponding to the particles settling at their stokes settling velocity, whereas if the flow were strongly turbulent we would expect $\beta = 0$, corresponding to them remaining well mixed within the plume. The introduction of this parameter allows for the possibility that all the particles will rain out of the flow in finite distance $X_{pf} = b_{p0}/(\beta\gamma)$ if $\beta > 0$. In (12) we have defined $\gamma \equiv U_s/U_{px}$ by analogy with the parameter γ defined in [10].

Assuming the concentration of particles is uniform over the thickness b_s, the mass flux of particles along the plume is found through consideration of the loss of particles $d\dot{m}_p$ that rain out from the base of the plume over a distance dX [11, 10]:

$$d\dot{m}_p = -U_s(\dot{m}_p/b_p)(dX/U_{px}) \tag{13}$$

Hence

$$\dot{m}_p = \dot{m}_{p0}\left[1 - \beta\gamma\frac{X}{b_{p0}}\right]^{1/\beta}. \tag{14}$$

In the case of well-mixed particles within the plume, so that $\beta \to 0$, (14) reduces to the exponential expression $\dot{m}_p = \dot{m}_{p0} \exp(-\gamma X/b_{p0})$, while for the laminar $\beta = 1$ case we would obtain a linear relationship: $\dot{m}_p = \dot{m}_{p0}(1 - \gamma X/b_{p0})$. The concentration of particles in the plume is given by (9)a and (14):

$$\phi_p = \dot{m}_p/(\rho_p Q_p) \tag{15}$$

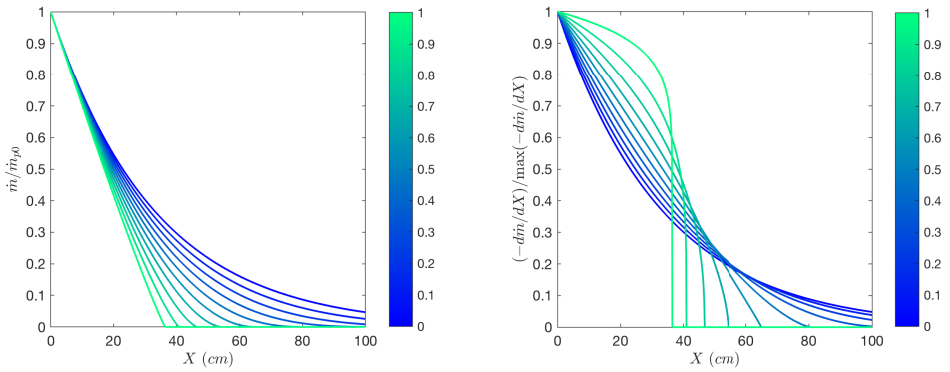

Figure 3: Normalised mass flux profile within the plume, varying beta. For $p_d =$ 64 μm, $\phi_0 =$ 0.01, $Q_0 =$ 50 cm^3/s.

The height of the sediment bed due to mass lost from the plume is given by:

$$h = \frac{-T}{\rho_p C} \frac{d\dot{m}_p}{dX} \tag{16}$$

where C is the particle packing fraction and T is the total duration of the experiment.

2.3 Sediment settling in return flow

Now we have an expression for the mass flux of particles leaving the plume, we consider how they are advected in the underlying ambient before either settling at the base or being re-entrained within the recirculating region. As we have already noted, there is some initial entrainment in the recirculating region with a volume flux given by (4), but negligible entrainment into the plume beyond $x = x_r$. Thus, to conserve volume for $x \geq x_r$ we require a return flow

$$U_r = Q_r/h_r = \frac{U_{r0}}{1 + sX/h_{r0}} \tag{17}$$

in which $U_{r0} = Q_{r0}/h_{r0}$, and, from (10), $h_{r0} = H_0 + sx_r - b_{p0} = 0.5(H_0 + sx_r)$. The path followed by a particle exiting the plume and setting in this flow is given by

$$\frac{dX}{dt} = -U_r, \qquad \frac{dZ}{dt} = -U_s, \tag{18}$$

Using (17) we obtain an implicit formula for the displacement (δ_x, δ_z) of a particle originating at $(X, h_r(X) \equiv h_{r0} + sX)$:

$$\delta_x^2 \frac{s}{2h_{r0}} + \delta_x \left(1 + \frac{s}{h_{r0}} X\right) - \frac{U_{r0}}{U_s} \delta_z = 0 \tag{19}$$

where of particular interest is the critical distance X_c for which all particles that leave the plume for $0 \leq X \leq X_c$ pass $X = 0$ before touching the bottom of the tank, and are thus entrained back into the recirculating region. Setting $X = X_c$, $\delta_x = -X_c$ and $\delta_z = -h_r(X)$ in (19) gives a quadratic expression for for X_c:

$$-X_c^2 \frac{s}{2h_{r0}} + X_c \left(\frac{U_{r0}}{U_s} s - 1\right) + \frac{U_{r0}}{U_s} h_{r0} = 0 \tag{20}$$

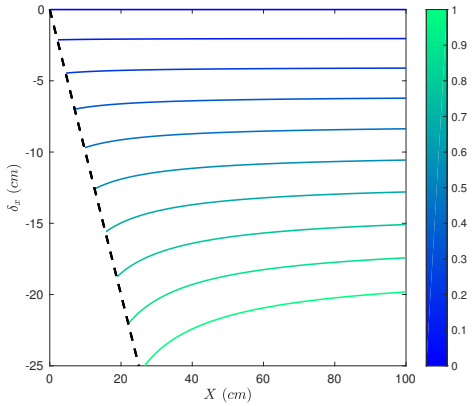

Figure 4: Displacement $\delta_x(X)$ due to particle advection in the return flow. Colour-scale indicates entrained volume (as a fraction of input volume flux Q_0) in the recirculating region, a proxy for return flow strength. Critical displacement $\delta_x = -X_c$ is denoted by the black dashed line. Calculated for $p_d = 64\ \mu m$, $\phi_0 = 0.01$, $Q_0 = 50\ cm^3/s$.

2.4 Sediment recycling

If a particle is lost from the flow at $X \leq X_c$, it will return to the recirculating region before being deposited at the base of the tank. The difference in plume particle mass flux at $X = X_c$ and $X = 0$ gives total mass of particles advected back to the recirculating region:

$$m_{r0} = m_{p0} - m_p(X_c) = m_{p0} \left(1 - \left[1 - \beta\gamma \frac{X}{b_p 0}\right]^{1/\beta}\right) \tag{21}$$

We assume that a fraction Δ is deposited within the recirculating region, and $(1 - \Delta)m_{r0}$ is added to the plume mass flux. This may be solved iteratively until the mass of particles sedimented out is equal to the mass flux into the plume.

3 Methods

3.1 Apparatus

The experimental setup is shown in Figs. 5 and 6. The main experimental tank is rectangular with width W=5 cm, length L=121 cm and height H=18.5 cm. At one end, a row of inlet pipes create an effective line source over the full width of the tank. The source is fed by a bucket of (usually fresh) particle-laden solution, which is kept well mixed with the use of a mechanical stirrer attached to a smart motor. A clear perspex slope is inserted above the source with the desired angle, creating a sloping ceiling up which the plume travels. An electroluminescent light sheet is placed below the tank, covering almost the full length, and a camera is mounted above. A camera is also mounted from the side to track the speed of the current and record the qualitative evolution of the flow.

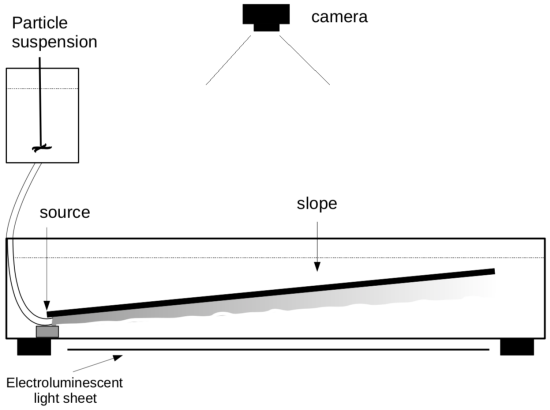

Figure 5: Side view of the experimental apparatus

3.2 Light attenuation technique and calibration

A non-intrusive method known as the light attenuation technique uses photographs taken before and after the experiment to measure the thickness of the particle bed. The experimental tank is illuminated from below using an electroluminescent light sheet, which provides a homogeneous light source over the majority of the tank area. The tank is photographed from above before and after each experiment. The light intensity I is related to the particle bed depth h by

$$I = I_0 + (I_0 - I_b)e^{-h/\sigma_{hl}} \tag{22}$$

where I_0 is the light intensity with no particles, I_b is effective "black" and σ_{bl} is the e-folding depth, which is measured. A calibration tank is also placed on the light sheet. Within the tank, a ramp of particles is created with a known bed depth, which is used to calculate σ_{bl} (Fig. 7).

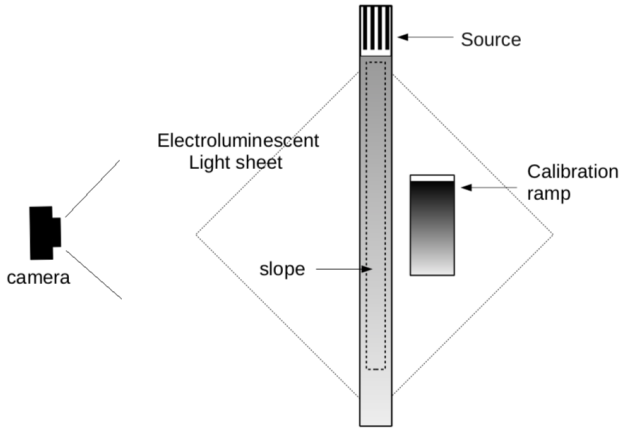

Figure 6: Top view of the experimental aparratus

3.3 Experimental procedure

The tank was first filled with room temperature seawater. The source pipes were flushed with fresh water, and put into place in the tank. The whole tank volume was then thoroughly mixed and the tank density ρ_t and free surface height h_t recorded. Next, freshwater of volume V_r and density ρ_r was added to the source reservoir, along with mass of particles m_p, and the solution thoroughly mixed. The first photo of the tank was then taken from above, and the slope inserted into the tank at angle θ. Recording of the experiment was commenced, from above and from the side, and the source was turned on to begin the experiment. Each experiment was run for a time T, typically limited by the available volume of the tank which filled over the course of each experiment, and then the source was turned off. Once the particles had settled to the base of the tank, the slope was removed and the final image taken from the above.

3.4 Experimental parameters

The key experimental parameters investigated were particle diameter, input particle concentration and slope angle. Particle diameter p_d was varied by using different particle size classes: 38–53 μm; 53–75 μm and 63–90 μm, which will hereafter be reported using the mid-points of the ranges (45, 64 and 76 μm). Particle concentration ϕ_0 was set to values of 1, 2 and 3 % by varying the mass of particles added to the plume mix, and the slope angle θ was varied over the range $2 \leq \theta \leq 10^\circ$ by manually adjusting the slope insert into the tank.

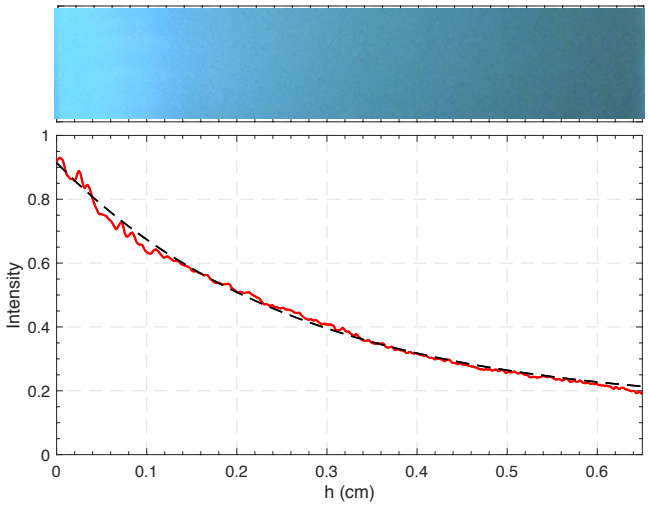

Figure 7: (upper panel) Image of the calibration tank used to calculate intensity for known particle depth. The pixels are averaged in the y axis to obtain the depth-intensity relation-ship. (lower panel) Depth-intensity calibration data (red) and fit using (22) (black dashed) for 45 μm particles.

4 Results

4.1 Velocity

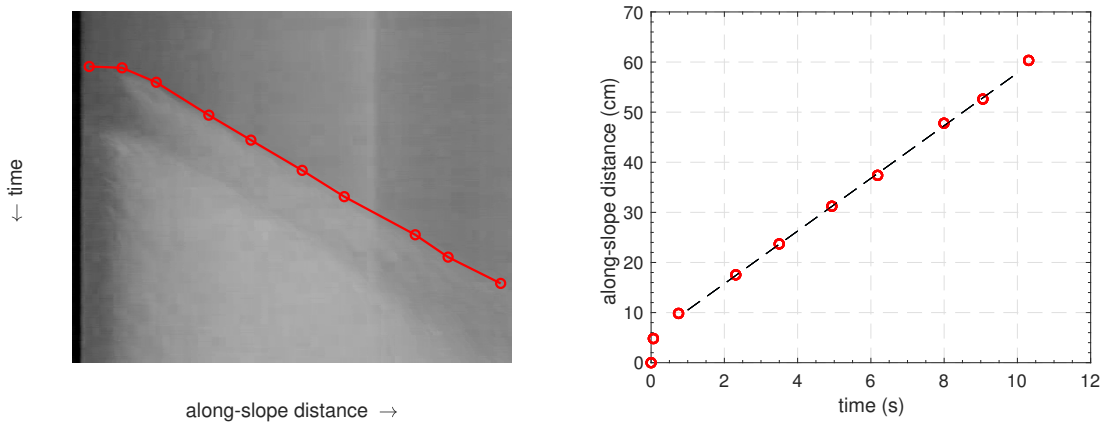

Figure 8: (left) Stacked along-slope segment of pixels from sequential images with front position picked out (red markers). (right) The same data with linear fit U_p.

The plume front position was measured by taking an along-slope slice through through sequential images of the side view of the tank during the initial phase of the experiment. These slices were stacked, giving a hovmoller-type view of the front position in time and space (Fig. 8a), and used to determine the steady state current speed U_p (Fig. 8b). After an initial adjustment period we found that the displacement was well described by a constant

Exp.	p_d (μm)	θ (°)	ϕ (%)	Q_0 (cm^3/s)	g_0' (m/s^2)	$(g_0'Q_f)^{1/3}$ (cm/s)	T (s)	τ (s)
1*	45	6.3	0.01	52	8.8	7.7	34	18
2	45	4.0	0.01	37	8.4	6.7	65	18
3*	45	3.8	0.01	33	9.3	6.7	59	18
4*	45	3.9	0.01	41	9.2	7.2	47	18
5*	45	2.0	0.01	53	7.8	7.4	45	18
6*	45	2.0	0.01	28	8.2	6.1	58	18
8	45	4.3	0.05	27	10.2	6.5	61	18
9	64	4.1	0.01	45	8.4	7.2	40	9
10	64	6.4	0.01	29	7.5	6.0	54	9
11	64	4.5	0.01	31	7.3	6.1	41	9
12	64	2.0	0.01	41	8.7	7.1	47	9
13	64	5.8	0.01	31	10.1	6.8	74	9
14	76	4.0	0.01	51	8.2	7.5	45	6
15	76	6.3	0.01	32	8.6	6.5	54	6
16	76	2.1	0.01	26	9.2	6.2	78	6
19*	45	6.4	0.01	54	8.8	7.8	42	18
20	64	4.0	0.02	45	8.0	7.1	40	9
22	64	3.9	0.03	55	7.9	7.5	48	9
23*	45	10.3	0.01	50	9.0	7.7	44	18
24*	45	4.0	0.01	59	72.8	16.3	38	18
25*	45	4.0	0.01	33	4.6	5.3	59	18
26*	45	4.0	0.01	53	46.9	13.5	33	18
28	64	4.0	0.03	56	10.1	8.3	40	9

Table 1: Experiments. Asterisk denotes $\tau/T > 1/3$ indicating results are expected to be strongly influenced by transient behaviour.

velocity. The initial phase was interpreted as being dominated by the source momentum M_0 of the flow, and thus U_p is given as the best fit to the data after this point.

Fig. 9 plots U_p against the velocity scale $(g_0' Q_f)^{1/3}$. Whilst a limited range of source conditions were used, the data show a linear dependence on $(g_0' Q_f)^{1/3}$ with a slope of 1.5, and do not show slope-dependence, both results of which are consistent with [4].

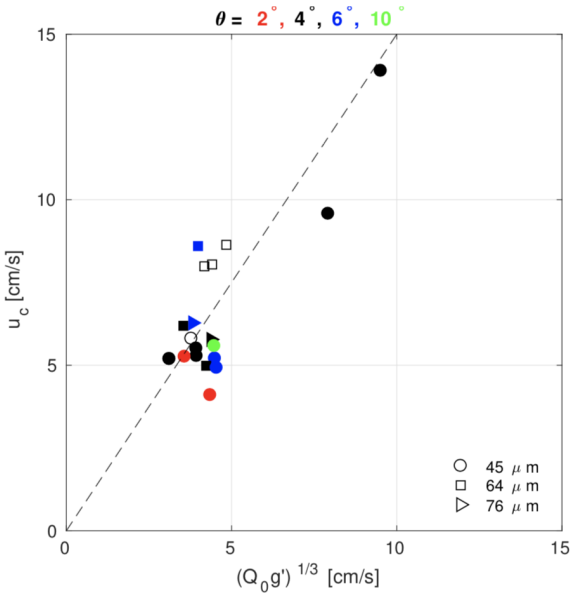

Figure 9: Along-slope front speed U_p against velocity scale against $(g_0' Q_f)^{1/3}$ for all experiments. The slope plotted $c = 1.5$.

4.2 Plume evolution

Fig. 10 shows the temporal evolution of the startup phase of a typical experiment. Once the source is turned on, the forced plume emerges into the experimental tank which is at this point extremely confined, and mixes over the full depth. The buoyant fluid that emerges from this region, which we term the recirculating region, then propagates along-slope. For a small p_d experiment such as that in Fig. 10, it takes some time for the particles raining out of the plume to reach the base of the tank, and at later time we observe that the descending particles are being advected back towards the source in the return flow. Finally, we note that some particles can be seen, still in suspension, at the top of the tank.

4.3 Particle Deposition

Figure 11 illustrates the dependence of the relative particle distributions on key experimental parameters. For fixed particle size and concentration, the shape of the distribution has no observable dependence on the angle of the sloping ceiling (Fig. 11). This is consistent with equation 14, where θ appears only as a geometric relationship between along slope flow

speed U_p and its x projection U_{px}: for the range of angles studied here ($2 \leq \theta \leq 10^\circ$), $\cos\theta$ varies by less than 1.5%.

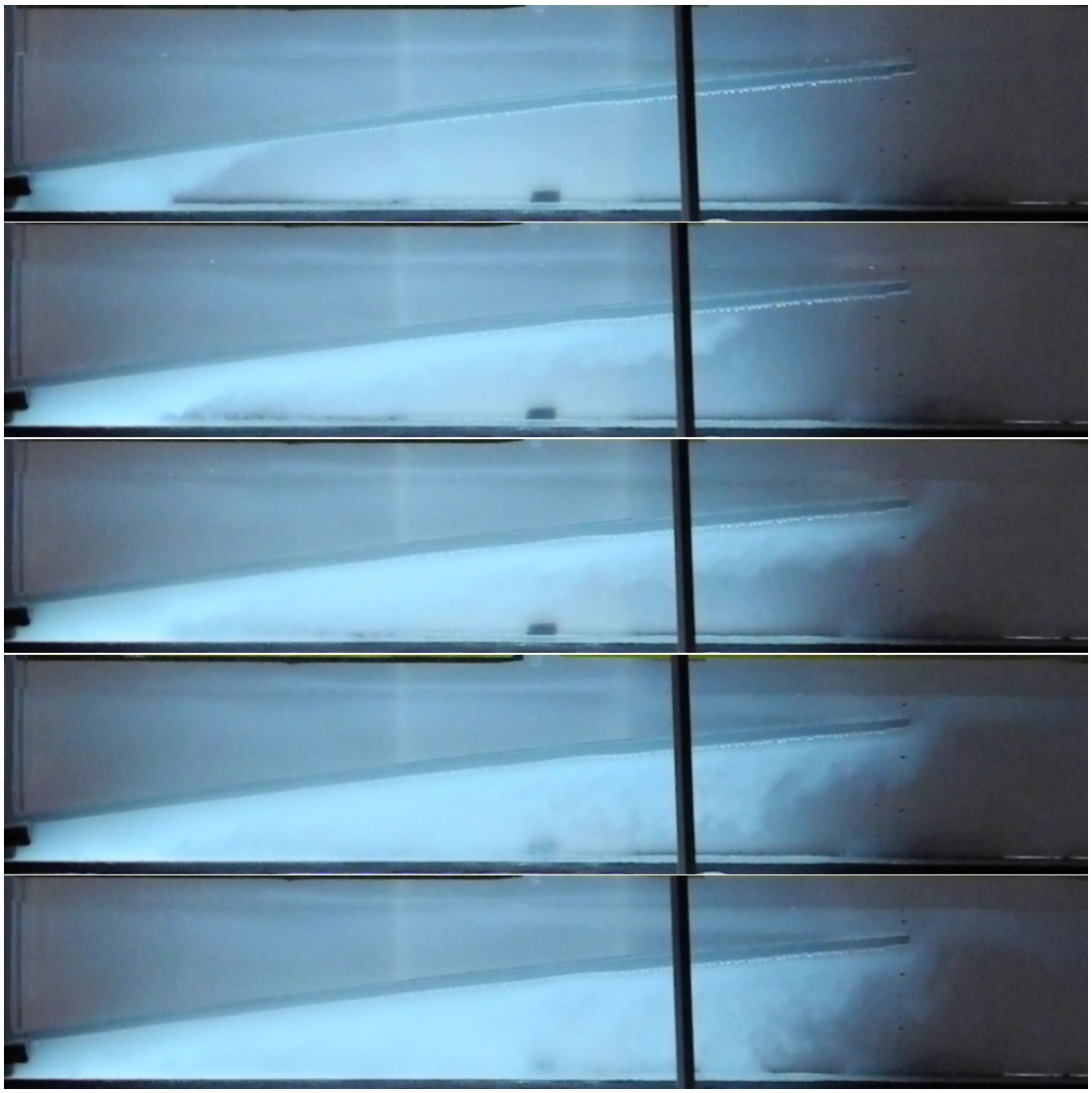

Figure 10: Sequence of images from Exp 2. Frames 1 and 2 are 8 seconds apart, and the subsequent frames are separated by 5 seconds.

The influence of particle diameter is also seen in Fig. 11 where the smaller particle size fraction has considerably shallower distribution of particles, indicating particles are remaining suspended within the flow for longer. This is consistent with expectations based on (14), where smaller particle diameter results in a slower stokes settling velocity. A key observation here is that we have a very "triangular" distribution of particles, especially for larger particle diameters. For 64 μm we also observe a cutoff distance X_{pf} beyond which no particles are deposited.

Finally we consider the influence of particle concentration. Few experiments were per-

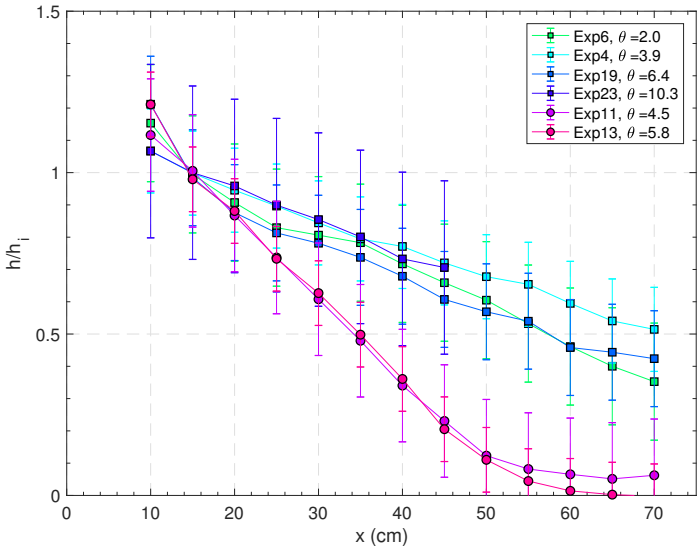

Figure 11: Normalised particle distribution for a suite of experiments varying slope angle for ϕ=0.01% and $p_d = 45$ μm (squares) and $p_d = 64$ μ (circles).

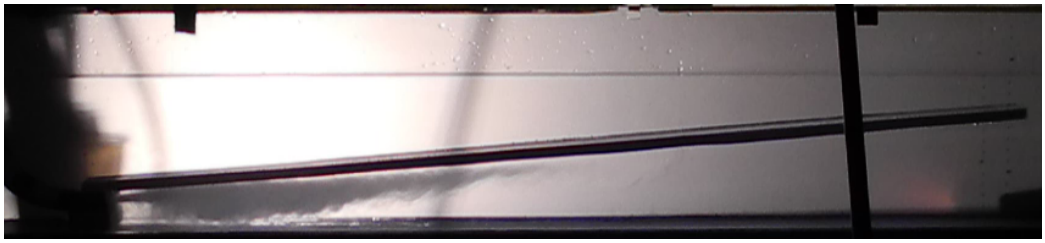

Figure 12: Snapshot of Exp. 20 showing the particle-free layer within the plume, adjacent to the slope and growing with along-slope distance.

formed at concentrations higher than 0.01% because of the experimental difficulty of keeping so many particles in suspension. Additionally, the high particle deposition rate meant that experiment length was limited by the thickness of the particle bed: too thick a bed absorbed all the source light and made the light attenuation technique impossible. From the experiments that were performed (Figure 13) we see no clear dependence of the normalised particle distribution on ϕ_0.

4.4 Application of theory

The theory derived in section 2 applies only to the plume at steady state, thus for it to be applicable we require that the particle deposition due to the startup phase, and due to the particles remaining in the plume once the source has been turned off, is much smaller than that due to the steady portion of the experiment. To test whether or not this is true, we compare the total duration of the experiment T to a timescale based on a particle settling at the stokes settling velocity though a typical plume width $\tau = b_{p0}/U_s$. Table 1 shows these values and highlights the experiments, predominantly those using the smallest particles,

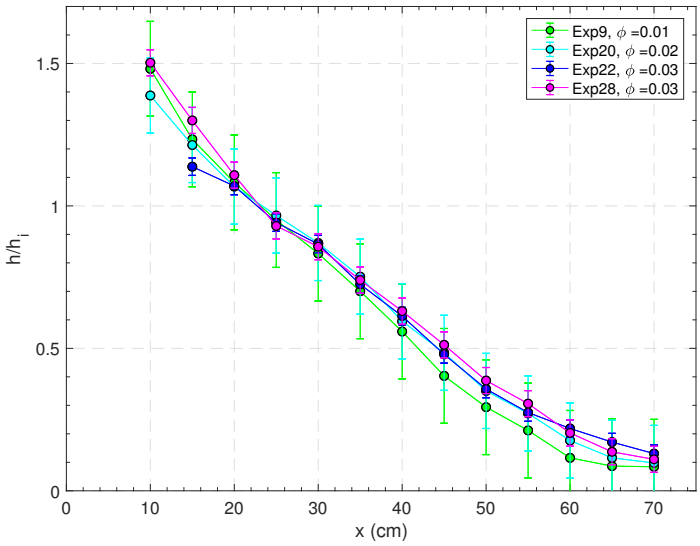

Figure 13: Normalised distributions varying concentration for 64 μm.

that are expected to be strongly influenced by transient behaviour.

4.4.1 Steady state

In order to apply the theory outlined in section 2 we first consider the experiments that are not affected by transient dynamics. There are two main unconstrained parameters in the theory. The first is β, describing how well mixed the plume is and allowing all the particles to rain out in finite distance. This is a feature of the experiments that is not consistent with a fully turbulent plume, in which the mass loss is exponential in x. The observed shape of the particle distribution, especially in the 64 and 76 μm experiments places a constraint on the value of β: as Fig. 3 shows, we require β $\sim$0.5 to obtain a triangular shaped-distribution.

The other unconstrained quantity is the amount of fluid that the plume entrains in the recirculating region, as this sets the strength of the return flow, and therefore the displacement of particles after they rain out of the plume. This is estimated to be on the order of the plume inflow Q_{r0} = const.Q_{p0} where the constant is taken to be 1 for most experiments.

Fig. 14 compares the experimental and model particle bed thicknesses, where the model is applied with and without the advection due to the return flow. The inclusion of the return flow allows the steepness of the particle bed thickness to be explained and greatly improves the model fit to the data. Fig. 15 applies the model to three different 64 μm experiments, reproducing the observed distributions extremely closely.

For the 76 μ m experiments, the model does not reproduce the data closely (Fig. 16). Using $p_d = 76$ μm, the model produces a particle bed that is far too steep. Fig. 16 shows the expected distributions for the upper and lower bounds of the particle size class: 63–90 μm. The stokes settling velocity scales with the square of the particle diameter (11), thus the ratio between the settling velocity of the 90 μm particles to the 63–90 μm particles within

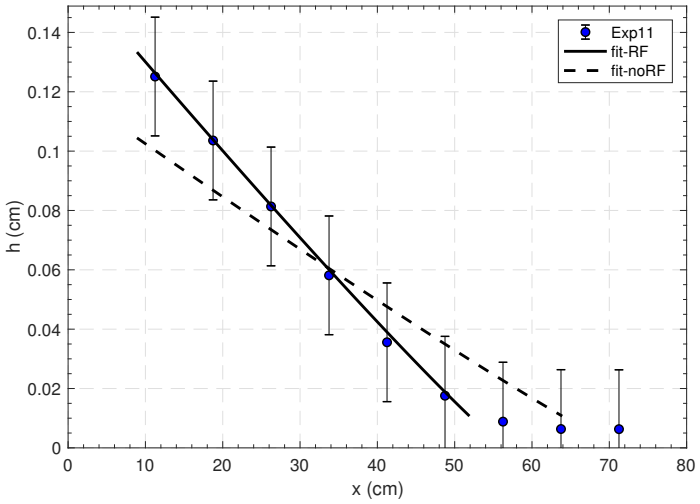

Figure 14: Dimensional particle distribution for experiment 11 and modelled distribution with and without the return flow. For $\beta = 0.55$, $Q_E = 0.8Q_0$.

the same size class is given by $(90/63)^2 \sim 2$. The inability of the model to reproduce the distribution using $p_d = 76$ μm may therefore be explained by the differential settling of particles of different diameter within the same size class. This effect may be highlighted in these experiments as this size class has a larger range than either the 45 or 64 μm classes.

4.4.2 Transient

For the experiments expected to be strongly influenced by transient behaviour, we also consider the mass of particles remaining within the plume after the source has been turned off. The mass is given by (14) and is assumed to settle directly downwards. Additionally, the steady state mass flux out of the plume is assumed to operate over a restricted interval $T - \tau$ (instead of T as in previous experiments).

For all the 45 μm experiments, the inclusion of the mass in the plume was extremely important to capturing the final sediment depth. Fig. 17 shows the total modelled height of the sediment, as well as the component that remained in the plume after the source was turned off. This component alone accounts for the majority of the deposited sediment. Of the sediment deposited during the experiment, it is clear that the return flow has a strong influence. The stepped feature at $x \sim 50$ cm shows the influence of the finite tank length: the model suggests that sediments raining out of the plume at the end of the tank should be advected all the way back to $x \sim 50$ cm before being deposited. Given the small proportion of the sediment bed conforming to the steady state dynamics, it is not possible to ascertain whether the data support this.

While good agreement between the data and the model is found in Fig. 17, the same is not true for many other 45 μm experiments. In several cases the model vastly over-predicts the final sediment depth, and in the case of Exp. 6 the shape of the sediment bed is not captured.

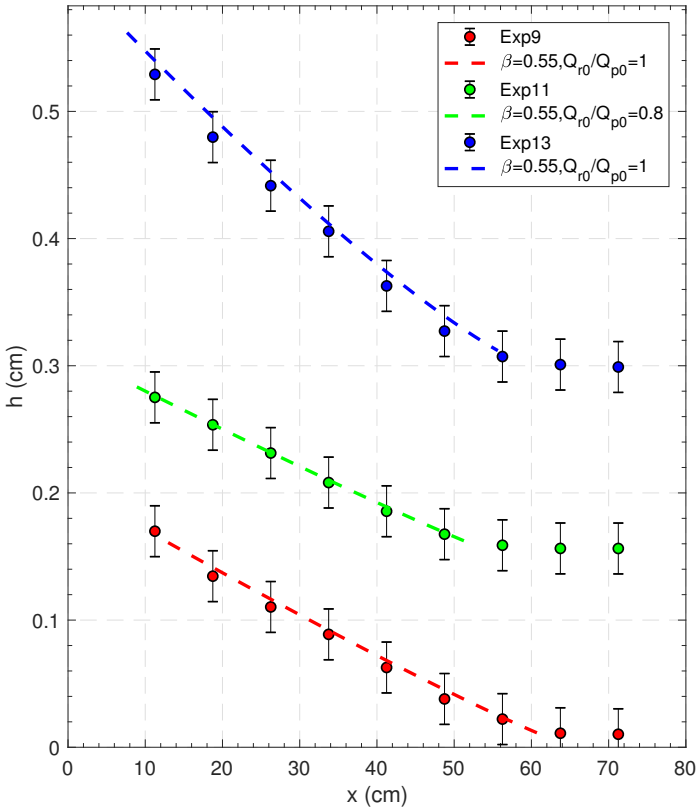

Figure 15: Dimensional particle distribution for several 64 μm experiments. Each curve has been offset by $h = 0.15$cm

5 Discussion

5.1 Geophysical considerations

The inclusion of the transient phase of the experiment, i.e. mass left in the plume at final time T, allowed us to take steps towards modelling the particle bed depth for the smallest particle class. However, these transient dynamics are unlikely to be important in a geophysical setting, where the plume operation timescale T is on the order of a month rather than $\sim$1 minute. The fact that the mass deposition from the transient part of the experiment was so much larger than that from the steady start part made it impossible to assess the validity of the steady state theory to these 45 μm experiments.

One process that we would expect to occur on geophysical scales, and that we neglected in our experiment, is entrainment into the plume. While this doesn't modify the plume velocity, it would act to increase the width of the plume and therefore modify deposition. In addition, if the plume were sufficiently angled, and entrainment sufficiently strong, particles could be re-entrained into the flow, a process that has been considered in other particle laden flows [13, 5].

Another such process is modification of plume buoyancy through particle deposition. We observed U_p to be constant, thus we did not need to consider this for our experiments,

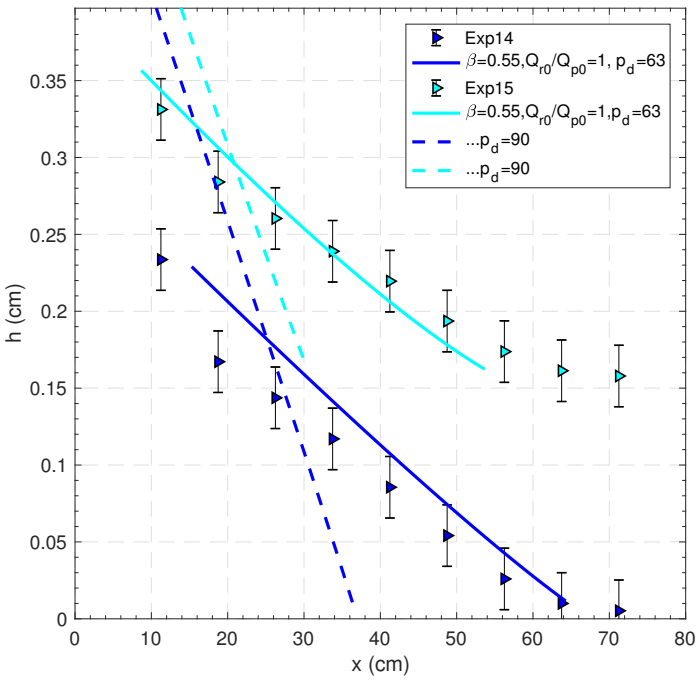

Figure 16: Dimensional particle distribution for experiment for two 76 μm experiments. Each curve has been offset by $h = 0.15$cm

however in cases where ϕ_0 is a large component of buoyancy and/or ϕ_p changes significantly as the plume propagates along-slope, modification of buoyancy through particle settling is expected to have a strong effect.

In these experiments our slope, or "ice" was both"non-thermodynamic" and "non-reactive", meaning it did not modify the plume properties by melting, as an ice shelf or tidewater glacier would. In situations where sub-glacial discharge is relatively large as compared to the volume flux from submarine melting, such as Greenland's tidewater glaciers in summer [12], this assumption is valid, however when melting is strong, the feedback between melting and plume buoyancy must also be considered.

Our experiments demonstrated that the return flow generated through entrainment of ambient fluid into the plume is an important process: only through including the advection of particles towards the source in the return flow were we able to capture the observed particle distribution. It is worth noting that this effect was particularly strong due to the line plume geometry that we used. In the case of a more isolated plume in a larger cavity, we expect that this effect would be smaller. However, both these cases (an isolated point source and a more distributed source) may be relevant: a recent study of Kangiata Nunata Sermia in South-west Greenland [8] inferred that a distributed source of buoyancy is the most likely configuration for this particular glacier.

Sediment wedges are commonly found at the grounding lines of both Greenlandic tidewater glaciers and Antarctic Ice Shelves, where they act to stabilise the grounding line [1]. They are thought to be the result of sub-glacially transported sediment. Our results suggest that the advection of sediments back towards the plume source by the return flow is another

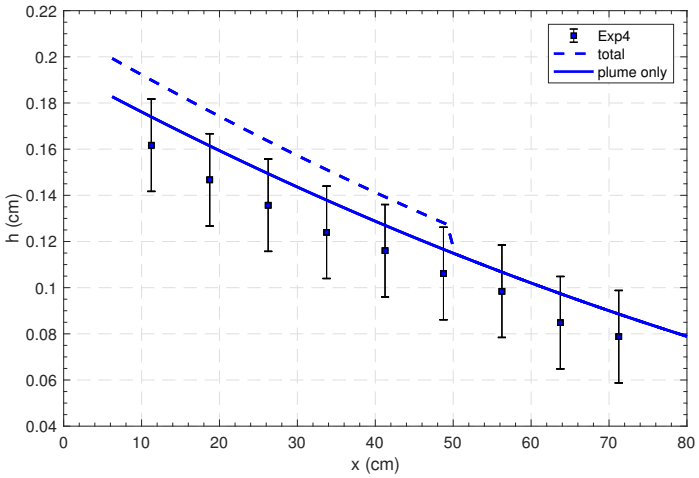

Figure 17: Dimensional particle distribution for Exp. 4 with $p_d = 45$ μm, showing the total modelled distribution and the contribution from the transient part of the experiment only.

possible mechanism for the creation of these wedges.

5.2 Settling model

A key observation from the experiments we performed was that the particles often did not remain well mixed within the plume, suggesting the flow was not sufficiently turbulent to keep them well mixed. The effect of this was accounted for using the parameter β, which allowed the model to behave either as turbulent (mixing dominated), fully laminar (settling dominated) or somewhere in between.

We can compare the relative importance of settling and mixing by comparing the time-scale for settling, $T_{settle} \sim b_{p0}/u_s$, and the time scale for mixing over the plume width, $T_K \sim b_{p0}^2/K$, where K is an eddy viscosity. Using the scale $K \sim u_\tau b_{p0}$, for turbulent channel flow, we find the ratio of time-scales:

$$\frac{T_{settle}}{T_K} = \frac{b_{p0}/u_s}{{b_{p0}}^2/K} = \frac{u_\tau}{u_s}$$

where u_τ is the friction velocity which may be estimated as a function of the free stream velocity (in this case plume velocity) as $u_\tau^2 = C_d u_p^2$, where an appropriate choice of the drag coefficient C_d for a hydraulically smooth surface is 2.5×10^{-3}. For a typical plume velocity of 6 cm/s, the friction velocity is $\sim$0.3 cm/s. For particle diameters 45–76 μm, u_s ranges from 0.17–0.47 cm/s yielding T_{settle}/T_K $\sim$1.8–0.6. The settling and mixing timescales are therefore of the same order for all experiments, explaining the "mixed" dynamics observed. This ratio also suggests that these experiments are applicable geophysical scenarios in which either the flow is relatively slow or particle diameter, and therefore settling velocity, is large.

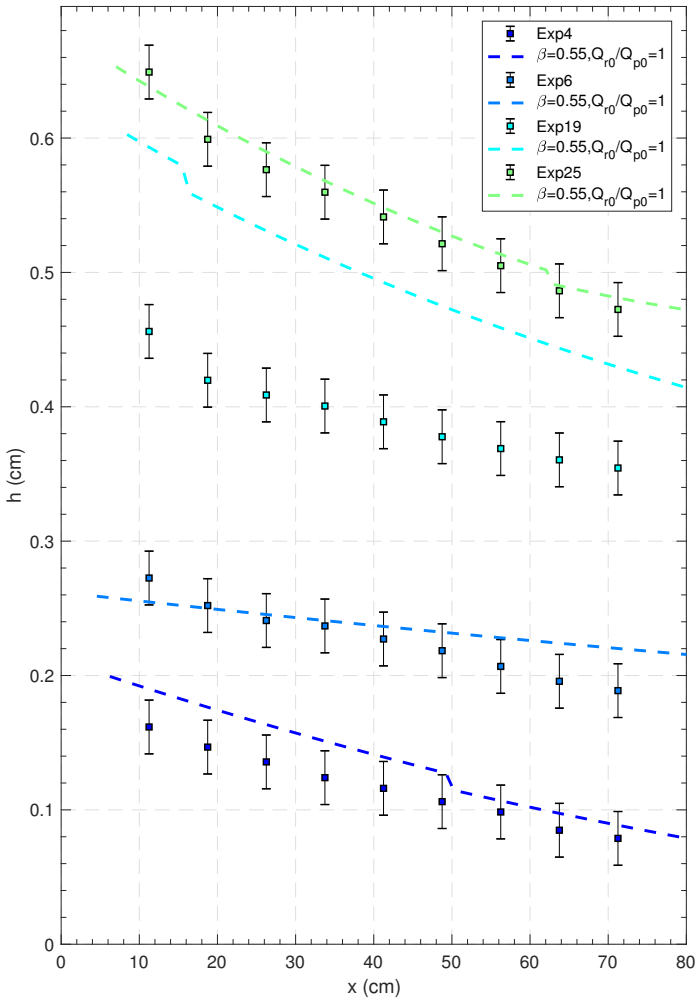

Figure 18: Dimensional particle distribution for several 45 μm experiments. Each curve has been offset by $h = 0.15$cm

6 Conclusion

In this study we performed laboratory experiments to investigate particle laden plumes travelling along an inclined ceiling; specifically the final distribution of particles deposited beneath the plume and how this distribution depended on slope, particle concentration and particle size. For the range of slope angles studied, $2 \leq \theta \leq 10°$, the final distribution was not observed to depend on slope. Particle size was shown to control the distribution through parameter $\gamma \equiv U_s/U_{px}$, moreover in order to explain some distributions we had to consider the range of particle diameters within a given particle size-class. The return flow generated by entrainment into the plume was found to advect particles back towards the source, and the inclusion of this process was necessary to capture the final sediment distribution.

7 Acknowledgements

Firstly, thank you to Bruce Sutherland, Claudia Cenedese and Craig McConnochie for sharing their time and invaluable expertise in the lab: it was a real pleasure working with you all! Thanks to Anders Jensen for his technical help and good cheer. Thanks to the lab crew for the swims and solidarity, the rest of the fellows for all the other fun. Finally, thanks to Mary-Louise Timmermans and Claudia Cenedese (this time with her director's hat on) for such an amazing opportunity.

References

[1] R. B. Alley, S. Anandakrishnan, T. K. Dupont, B. R. Parizek, and D. Pollard, *Effect of sedimentation on ice-sheet grounding-line stability*, Science, 315 (2007), pp. 1838–1841.

[2] R. T. Bonnecaze, H. E. Huppert, and J. R. Lister, *Particle-driven gravity currents*, Journal of Fluid Mechanics, 250 (1993), pp. 339–369.

[3] R. T. Bonnecaze and J. R. Lister, *Particle-driven gravity currents down planar slopes*, Journal of Fluid Mechanics, 390 (1999), pp. 75–91.

[4] R. E. Britter and P. F. Linden, *The motion of the front of a gravity current travelling down an incline*, Journal of Fluid Mechanics, 99 (1980), pp. 531–543.

[5] G. G. Ernst, R. S. J. Sparks, S. N. Carey, and M. I. Bursik, *Sedimentation from turbulent jets and plumes*, Journal of Geophysical Research: Solid Earth, 101 (1996), pp. 5575–5589.

[6] A. Jenkins, *A one-dimensional model of ice shelf-ocean interaction*, Journal of Geophysical Research: Oceans, 96 (1991), pp. 20671–20677.

[7] R. Mugford and J. Dowdeswell, *Modeling glacial meltwater plume dynamics and sedimentation in high-latitude fjords*, Journal of Geophysical Research: Earth Surface, 116 (2011).

[8] D. Slater, P. Nienow, A. Sole, T. Cowton, R. Mottram, P. Langen, and D. Mair, *Spatially distributed runoff at the grounding line of a large greenlandic tidewater glacier inferred from plume modelling*, Journal of Glaciology, 63 (2017), pp. 309–323.

[9] J. Smith, T. J. Andersen, M. Shortt, A. Gaffney, M. Truffer, T. Stanton, R. Bindschadler, P. Dutrieux, A. Jenkins, C.-D. Hillenbrand, et al., *Sub-ice-shelf sediments record history of twentieth-century retreat of pine island glacier*, Nature, 541 (2017), p. 77.

[10] K. Snow and B. Sutherland, *Particle-laden flow down a slope in uniform stratification*, Journal of Fluid Mechanics, 755 (2014), pp. 251–273.

[11] R. S. J. Sparks, R. T. Bonnecaze, H. E. Huppert, J. R. Lister, M. A. Hallworth, H. Mader, and J. Phillips, *Sediment-laden gravity currents with reversing buoyancy*, Earth and Planetary Science Letters, 114 (1993), pp. 243–257.

[12] F. Straneo and C. Cenedese, *The dynamics of greenland's glacial fjords and their role in climate*, Annual Review of Marine Science, 7 (2015), pp. 89–112. PMID: 25149564.

[13] B. R. Sutherland and Y. S. D. Hong, *Sedimentation from particle-bearing plumes in a stratified ambient*, Physical Review Fluids, 1 (2016).